Experiments in Fluids (2025) 66:160
https://doi.org/10.1007/s00348-025-04083-0

RESEARCH ARTICLE

PIV in the vicinity of cork samples in particle-laden high-enthalpy flow

Ciro Salvi[1] · **Ali Gülhan**[1]

Received: 28 January 2025 / Revised: 10 June 2025 / Accepted: 11 July 2025

Abstract

This research aims at analysing the particle-laden flow of the high-enthalpy wind tunnel L2K, which is used to characterize the impact of dust particles on the recession behaviour of thermal protection systems during Martian entry flight. In the tests, a slightly simplified Martian atmosphere (97% CO_2 and 3% N_2) is used. The high-enthalpy flow is loaded with micrometric particles of magnesium oxide. Several samples for stagnation point tests made of P50 cork are positioned inside the particle-laden flow. The particles' mean velocity is measured at the stagnation point of the probe in a region of interest that includes the free stream and the shock layer, with a 2D-2C particle image velocimetry (PIV) system. Several particle flow features are observed, such as the particle's steep velocity gradient across the shock, the shock layer, and a counter-flow that might be caused by outgassing and rebounded particles. Average particle velocities ranging from 0 to 2100 m/s are measured and compared with the numerical simulation of the wind tunnel's particle-free flow. A discussion on particle agglomeration due to melting is reported, and the importance of considering this effect for the simulation of atmospheric entry in particle-laden atmospheres is highlighted. Particles are collected with double-sided copper tape on a cooled probe and analysed with a scanning electron microscope (SEM) and with energy-dispersive X-ray spectroscopy (EDX), to characterize their morphological change during their residence time in the wind tunnel flow.

Graphic abstract

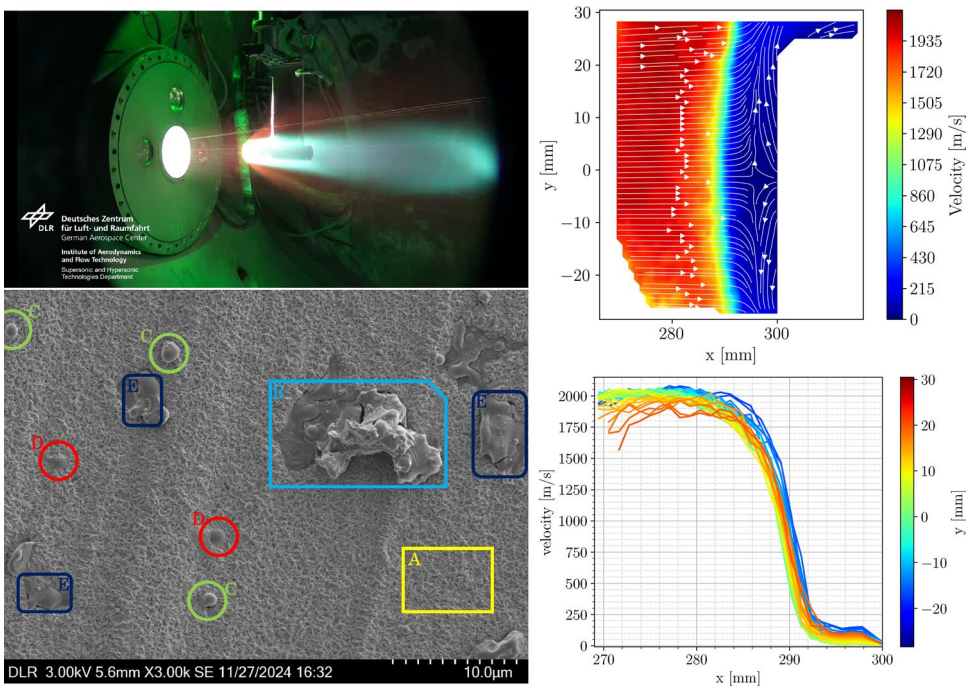

Extended author information available on the last page of the article

Published online: 05 August 2025

1 Introduction

An ongoing collaboration between the German Aerospace Center (DLR) and NASA Ames Research Center focuses on studying the heat flux augmentation and erosion on thermal protection systems (TPS), due to the presence of suspended dust particles during atmospheric entry on Mars. To increase the reliability of the numerical simulations of Martian landers, the collaboration aims at improving the mathematical modelling and numerical rebuilding of two-phase hypersonic high-enthalpy flows by comparison and validation with experimental data. Past experiments at DLR were performed in the GBK supersonic wind tunnel and in the L2K arc-heated wind tunnel, at the Supersonic and Hypersonic Technologies Department of DLR in Cologne.

The particle-laden supersonic flow created in the GBK was thoroughly studied and characterized in Allofs et al. (2022, 2023a, 2023b) by shadowgraphy and particle tracking velocimetry (PTV): particle velocity and size were measured, and heat flux augmentation was observed on the probes inserted in the two-phase flow. Based on this knowledge, additional research is being performed in the L2K arc-heated wind tunnel to include high-enthalpy effects, thus increasing the accuracy of the Martian atmospheric entry simulation in ground testing facilities. Particle-enhanced heat flux was observed in the L2K in German Aerospace Center (DLR) and European Space Agency (ESA) (2006), where a particle-laden flow at supersonic/hypersonic speed was created for the first time in the wind tunnel. The L2K flow characterization continued in Salvi et al. (2023), where Tunable Diode Laser Absorption Spectroscopy (TDLAS) was applied and analysed. In Salvi and Gülhan (2024), the L2K was upgraded to generate particle-laden flows with a slightly simplified Martian atmosphere for long testing times, suitable for TPS characterization (several minutes). The particle-laden flow was studied with particle image velocimetry (PIV), and the repeatability of the two-phase flow conditions was verified. PIV was applied for the first time in a wind tunnel of this kind. Particle velocities of more than 2000 m/s were measured in the free stream.

This paper aims to deepen the understanding of particle-laden high-enthalpy flow in the L2K wind tunnel by particle flow characterization. The insights gained from this study advance the current knowledge of the wind tunnel's flow and offer valuable interpretative tools for future research focused on material response characterization and on numerical models' validation for this environment. The following sections present the results of an investigation into the qualitative behaviour of cork samples exposed to the particle-laden high-enthalpy Martian atmosphere simulated in the L2K wind tunnel and focus on characterizing particle velocity around the samples by means of PIV and on observing collected particles with an electron microscope. Multiple tests were performed on different samples to evaluate the repeatability of the experiments and to qualitatively examine the effects of the particles. The analysed flow conditions were defined by DLR in the post-flight data-analysis of ExoMars 2016 and are reported in Table 1. Micrometric particles of MgO are used for all testing in this work.

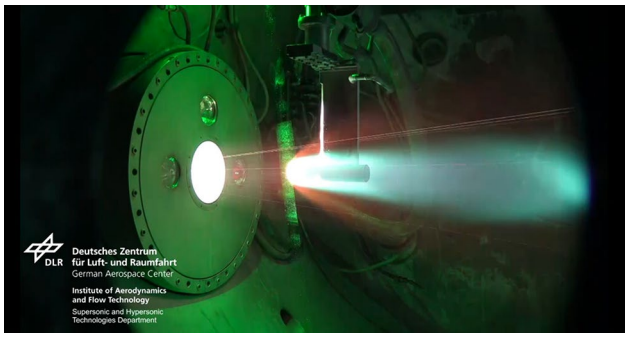

Fig. 1 Particle-laden flow test in L2K: PIV is implemented upstream of a cork sample

Table 1 Flow conditions FC. *P* and *nP* superscripts indicate the FC with and without particles, respectively. The mass flow rates are equal for all FC

Parameter	FCI^{nP}	$FCII^{nP}$	FCI^{P}	$FCII^{P}$
Reservoir pressure, [hPa]	790	930	790	930
MgO Particles	✗	✗	✓	✓
Predicted specific enthalpy*, [MJ/kg]	5.6	9.2	5.6	9.2
Predicted reservoir temperature*, [K]	2815	3283	2815	3283
Total mass flow rate, [g/s]	41.2			
Mass flow rate CO_2 (97%), [g/s]	$38^{hot}+2^{BP}$			
Mass flow rate N_2 (3%), [g/s]	1.2^{hot}			

*Estimated with quasi-1D flow solver NATA (Bade and Yos 1975)

PIV is implemented to monitor the particle flow and to measure particle velocity in the shock layer and in the free stream at the same time. Figure 1 shows a test in the L2K wind tunnel, with particle-laden flow: the flow comes from the left; the sample is positioned inside the flow with a cooled support; a bright red-orange bow shock is generated when particles are present, and a blue-greenish wake including ablation products is observable. One can see the green light sheet used for PIV that highlights the particles suspended in the flow. The region of interest for PIV is a 4.9 cm × 5.8 cm region upstream of the stagnation point.

Some particles are collected inside the flow, with the goal of studying their morphology to better characterize the

particle-laden flow conditions. Although conceptually simple, particle collection in high-enthalpy flows is challenging. Particle samples were collected in high-enthalpy flows in Saile et al. (2020), where a probe was developed ad-hoc for collecting alumina from solid rocket combustion, following the idea of Kessel (1987). The probe was cooled and had an internal spray system that could collect the particles in a liquid sample, which would then be analysed. Developing such a probe for particle collection in the L2K is very challenging, and a simpler technique is preferred at this stage of the study. In a recent publication, double-sided carbon tape was used to collect particles from a green propellant thruster plume in Buntrock et al. (2023), and the collected samples were then analysed with a scanning electron microscope (SEM). This technique is selected as a good compromise between simplicity and effectiveness for the L2K particle-laden flow. Collected particles are analysed via SEM and energy-dispersive X-ray spectroscopy (EDX). MgO particles were observed with a SEM in Wang et al. (2020), confirming the feasibility of this imaging technique for the selected chemical species. Due to the intrusivity and the limitations of this technique, this analysis can give qualitative hints on the particles' morphological change during flight, but it cannot be used for the determination of particle size with image post-processing, as presented for example in Langton and Hermansson (1973). In this way, the phenomenon of agglomeration of the particles due to melting hypothesized in Salvi and Gülhan (2024) is further investigated. From now on, the agglomeration due to melting will be referred to as ***agglo-melting***, and a molten agglomerate will be referred to as *agglo-molten* particle.

In the following sections, the L2K arc-heated facility and the experimental setup will be presented; then, the experimental results will be reported and discussed; finally, conclusions and outlook will be given.

2 Arc-heated facility L2K

As reported in Salvi and Gülhan (2024), L2K is an arc-heated continuous-flow high-enthalpy wind tunnel suited—for instance—for TPS materials testing and components' demisability tests, as it can provide high heat fluxes for long testing times, at the expense of aerodynamic properties characterization: the low density environment causes Reynolds number to be too low compared to atmospheric entry. In such conditions it is important to consider a reacting non-equilibrium flow. L2K reservoir is energized by a 1.4-MW Huels-type arc heater which grants the flow a high specific enthalpy thanks to the electrical discharge. Flow conditions can be varied with different degrees of freedom, such as mass flow rate, reservoir pressure, nozzle exit diameter, sample position, and chamber background pressure, which grant a wide range of operating conditions of the testing facility. Heat flux varies also on the flow axis, thanks to the nozzle's geometry that causes flow post-expansion, giving an additional degree of freedom when designing a wind tunnel condition. A broad selection of intrusive and non-intrusive measurement techniques can be used (for instance, thermocouples, infrared cameras, pyrometers, Pitot probes, tunable diode laser absorption spectroscopy or TDLAS, laser-induced fluorescence or LIF, Fourier transform infrared spectroscopy or FTIR, PIV).

The analysed flow conditions (FC) are defined by DLR in the post-flight analysis of ESA ExoMars 2016 mission ESA (2016) and are reported in Table 1. Here, the superscript "*P*" indicates the flow condition with particles, while the superscript "*nP*" indicates no particles in the flow. The wind tunnel flow represents a slightly simplified Martian atmosphere, and its composition is 97% CO_2 and 3% N_2 in mass. To generate the particle-laden flow, a seeding generator inserts MgO particles in the L2K flow upstream of the nozzle expansion. The seeding generator is a pressurized vessel working with a bypass (BP): to keep the mass flow rate as specified in Table 1, 38 g/s of CO_2 is heated in the arc heater together with 1.2 g/s of N_2 (superscript "*hot*"), while 2 g/s of CO_2 is used for collecting the particles inside the pressurized vessel (superscript "*BP*"). Particles of magnesium oxide (MgO) are stored inside the pressurized vessel. The used particles are LUVOMAG®M SF. 95% of them range between 1 μm and 3 μm, as specified by the producer. According to Palmer et al. (2020, 2022), this size range is valuable for generating representative data for Martian entry studies.

L2K nozzle geometry to be used is reported in Fig. 2.

3 Experimental setup

This section describes the used samples, the particle collection technique, and the PIV setup.

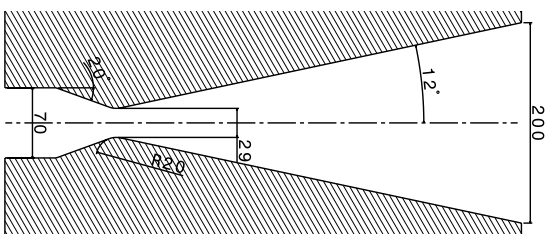

Fig. 2 L2K nozzle geometry, 200-mm exit diameter configuration. Sizes in mm

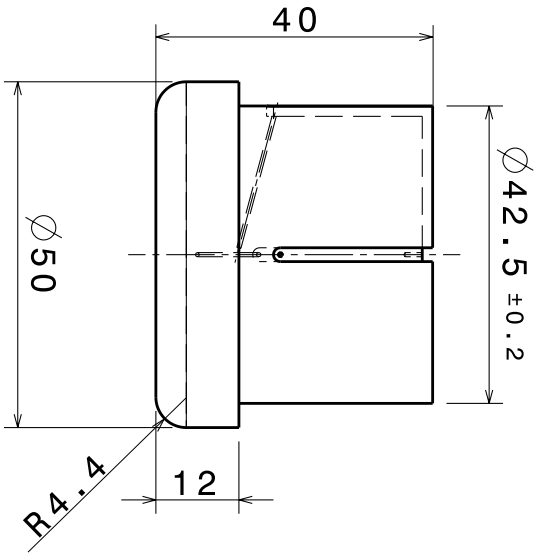

Fig. 3 Sample geometry. The left side faces the flow; the right thinner side is used to position the thermocouples and to connect to the cooled support

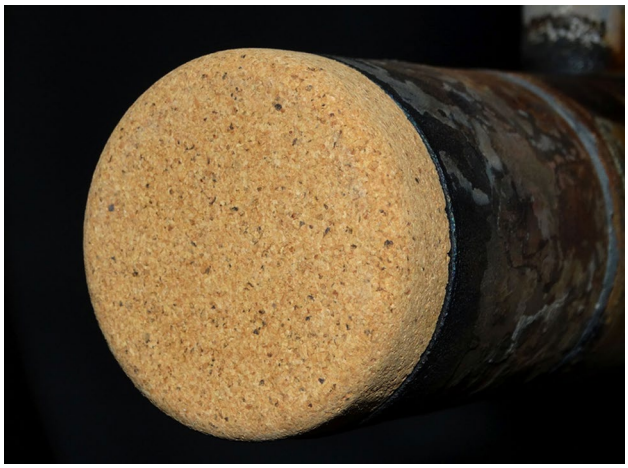

Fig. 4 Sample before testing

3.1 Cork samples

The samples used in this study all have the same characteristics, to address the repeatability of the tests in the L2K wind tunnel. All tests are executed in the same way, and the only variables between tests are the reservoir pressure and the presence of particles, as reported in Table 1. The sample geometry is presented in Fig. 3. The material is P50 cork, from the company Amorim Cork Composites (Amorim 2025). The selection of P50 as the test material is supported by the extensive availability of its thermal properties in the literature, as well as by the historical use of cork composites like Norcoat Liege in the heat shields of past Martian landers, such as for Schiaparelli (ESA 2016). Future studies should investigate the behaviour of alternative materials, such as the carbon-based ZURAM.

During a wind tunnel test, the sample is positioned on flow axis after the flow is stabilized, at a distance of $x = 300$ mm from nozzle exit. At this location and with the selected geometry, the predicted heat flux and stagnation pressure are, respectively: 280 kW/m^2 and 1280 Pa for FCI^{nP}, and 490 kW/m^2 and 1510 Pa for FCII^{nP}. The residence time in the flow is set to 60 s. A total of 10 tests are performed, namely 2 tests per each FC^{nP} and 3 per each FC^{P}, to assess repeatability. The campaign showed very repeatable results in terms of PIV, so only one test per flow condition is reported in Sect. 4. A picture of the sample installed in the wind tunnel before the test is shown in Fig. 4.

Several pictures and scans are taken before and after each test to observe the geometric change of the sample and to monitor the erosion. During the test, two infrared cameras monitor the surface temperature from the side and from the front, and two pyrometers monitor the temperature on the centre of the sample. Four embedded thermocouples monitor the in-depth temperature. Three video cameras record the test from different perspectives and with different zooms. Thermal data and 3D scans are not reported in this work, as they fall outside of the scope of the paper that instead focuses on the particle-laden flow characterization around the cork samples. The results of the material response analysis will be reported in a follow-on work. Flow characterization is performed by means of particle collection and PIV, which are discussed in the next sections.

3.2 Particle collection

Particles are collected with the double-sided copper tape used for electron microscopes. A water-cooled stagnation probe made of copper is used as support for the copper tape strip, which is positioned inside the flow at the same location of cork samples. The cooled support has the same geometry of the cork samples described before. To collect the particles, the probe is moved inside the particle-laden flow with a shield. Once it reaches the axial position, the shield is quickly removed (tenths of a second), and the collection process begins. After a residence time of 2 s, the shield is positioned again in front of the sample, and the probe is then removed from the flow. The residence time inside the flow is limited by the high heat flux: in FCII^{P} the heat flux is so intense that the collection tape melts if the probe is left inside for more than 2 s. The same method can be used for longer times in FCI^{P} that provides lower heat flux.

A control sample of particles before the injection in the wind tunnel is observed with the SEM, as presented in Fig. 5. The observation of the control sample is important for

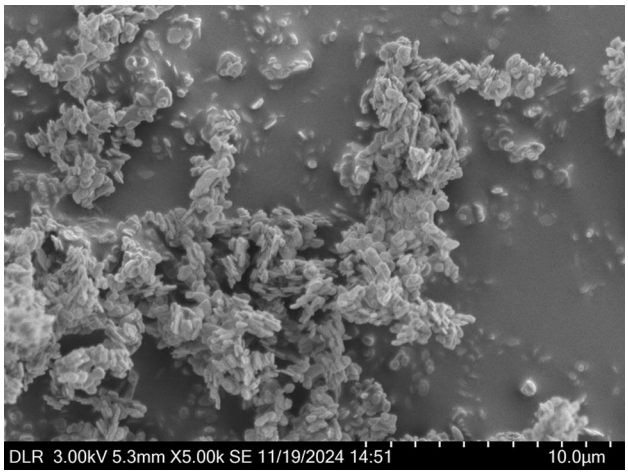

Fig. 5 Magnesium oxide particles before testing

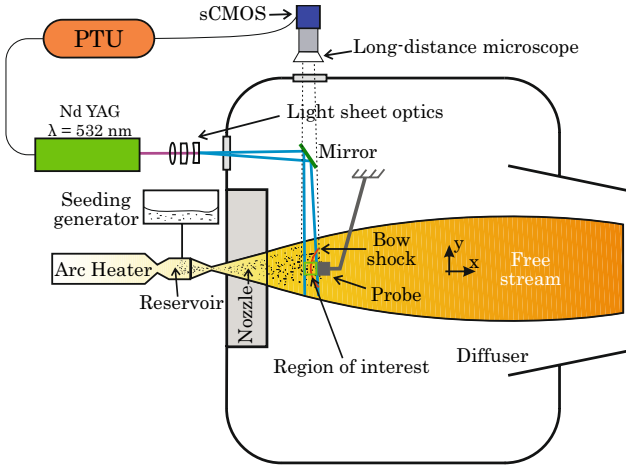

Fig. 6 Experimental setup sketch. The reported axes originate on flow axis, at the nozzle exit location. In practice, both the seeding generator and the sCMOS camera are positioned in the *xz* plane

the comparison with the samples collected in the stagnation point, helping to understand physical phenomena that the particles are subject to, during their flight in the wind tunnel and after impact. In the control sample, one can observe the particles' uniform size distribution of approximately 1 µm and their disc-like shape.

Particle collection is considered here a valuable straightforward method for analysing particles and gaining insight into the complex physical processes they experience: the passage in the high-temperature reservoir of the wind tunnel, the possible phase change and agglomeration, and the impact on the probe. However, the described technique generates a high thermal and mechanical load on particles at impact, causing a morphological change, which can be due to melting, agglomeration, sintering, or disintegration. Moreover, depending on the Stokes number of the particles, they are collected with different efficiency by the probe, depending on their size: a small particle can easily follow the streamlines downstream of the bow shock, and it will tend to pass over the probe, while a bigger particle will most likely impact the probe, getting collected by the adhesive strip. This intrusive technique is thus intended for qualitative analysis only.

3.3 Particle image velocimetry (PIV)

A 2D-2C PIV setup is implemented as sketched in Fig. 6 to measure particle velocity. As reported in Salvi and Gülhan (2024), a significant velocity lag exists between particle and flow velocities, meaning that the measurements presented in this paper should not be interpreted as representing the flow velocity.

The PIV hardware, consisting of the programmable timing unit (PTU), the dual-cavity laser, and the sCMOS camera, is described in Salvi and Gülhan (2024). The camera is positioned outside of the test chamber for easier access, and it is equipped with a long-distance microscope. A comprehensive description of PIV experimental technique can be found in Raffel et al. (2018).

The coordinate system is defined as follows: the x-axis coincides with the nozzle symmetry axis, it originates at the nozzle exit, and x values are positive downstream (towards right, referring to the picture); the y-axis defines the transversal direction, it originates on flow axis, and y values increment towards the top of the wind tunnel; both axes belong to the laser sheet plane. Note that the sCMOS is represented on a wrong plane for schematic visualization purposes only; same for the particles injection, which happens on the horizontal mid-plane of the settling chamber. In practice, both the seeding generator and the sCMOS camera are positioned in the xz plane.

The light beam is focused on the flow axis and converted into a light sheet using a cylindrical lens (f = -200 mm). This light sheet plane coincides with the xy plane, and its thickness is approximately 1 mm. It is redirected by a mirror towards the flow axis and the region of interest, aligning with nozzle axis which lies within the light sheet plane. The light sheet illuminates the region downstream of the nozzle exit, from approximately $x = 260$ mm to $x = 315$ mm.

The long-distance microscope is used to provide a high resolution at a distance higher than 1.5 m. A narrowband filter is positioned in front of the objective, with $FWHM = 5$ nm around 532 nm to increase the signal-to-noise ratio. The imager observes the light sheet plane perpendicularly. It has a 6.5 µm pixel size and a 2560×2160 px^2 maximum resolution. The minimum achievable interframing time is 120 ns. The field of view is 58.0 mm × 49.1 mm; thus, the image resolution is 44.0 px/mm. The whole image is used in PIV evaluation. The "short side" of the camera (2160

px) is positioned parallel to the nozzle axis; in this way, the whole bow shock in front of the probe and the region around its shoulder can be observed. In Fig. 7, the raw data (two subsequent frames) of a sample picture are presented. On the right of both frames, one can observe the profile of the stagnation sample, which is highlighted by the laser sheet. In the remaining part of the images, the particles illuminated by the laser are visible. The repetition rate is 15 Hz. With a residence time of 60 s, the total amount of PIV images is 900 for each test.

Based on Salvi and Gülhan (2024), the expected particle speed is approximately 2 km/s. Due to the large expected velocity gradients across the bow shock (from more than 2000 m/s to 0 m/s), a compromise must be made on the choice of the interframing time, to resolve both the free stream velocity and the shock layer velocity in an acceptable way. Therefore, an interframing time of $\Delta t = 1\,\mu s$ is selected, even though this results in an estimated free stream particle displacement of 2 mm between frames, corresponding to roughly 88 pixels—which is considered a large displacement the PIV community.

3.3.1 PIV processing strategy

Data processing is made with the DaVis software's built-in functions. The raw images are first transformed from pixels to millimetres thanks to the calibration image taken before the experiments. They are then pre-processed to remove the background and normalize the particles' signals with DaVis built-in function "Image Preprocessing", based on local averaging and normalization.

The challenge of performing a PIV evaluation in this region lays in the very high dynamic range of the particles and the different types of particles that can be observed. They can come from different locations like the settling chamber of the wind tunnel (where particles are inserted) or the sample itself (consider for instance the erosion phenomenon). One can observe:

- *Nominal particles* looking like the control sample (Fig. 5), coming from the settling chamber: they are the fastest particles, as they have micrometric size, thus a low Stokes number.
- *Particle agglomerates* coming from the settling chamber: they travel at lower velocities compared to nominal particles. They have no upper limit in size and can be big chunks.
- *Particle droplets* coming from the settling chamber: they are nominal particles which experience phase change.
- *Agglo-molten particles* coming from the settling chamber: they are agglomerate of particles which experience phase change.
- *Rebounded particles* coming from the settling chamber: they "bounce" on the sample and their size is unknown, since what happens after impact is undefined. They can be seen moving in the opposite direction of the flow, usually with low velocity, and can cross the bow shock. They can be large, dragging the PIV evaluation towards the computation of negative results.
- *Eroded particles* coming from the sample due to erosion processes.
- *Outgassed particles* coming from the sample and being pushed in the counter-flow direction by the outgassing phenomenon.

In addition to the different nature of the particles, different regions of the analysed images can be defined, as sketched in Fig. 8. From upstream to downstream one can find:

- *Free stream*: it has a very high velocity and contains primarily nominal particles, along with occasional agglomerates, droplets, and rebounded particles.
- *Bow shock*: it is the region where a discontinuity of the physical properties of the flow happens, and it is where the nominal particles start to slow down. In this region a larger amount of rebounded/eroded particles can be found.
- *Shock layer (including boundary layer)*: it is the region downstream of the bow shock; here, all types of particles can be found. In the shock layer one can observe:
  - *Stagnation region*: it is the region right in front of the probe very close to its axis, in the vicinity of the stagnation point, where the flow velocity is zero.
  - *Shoulder region*: it is the region across the corner of the sample, where the particles re-accelerate following the expanding flow.

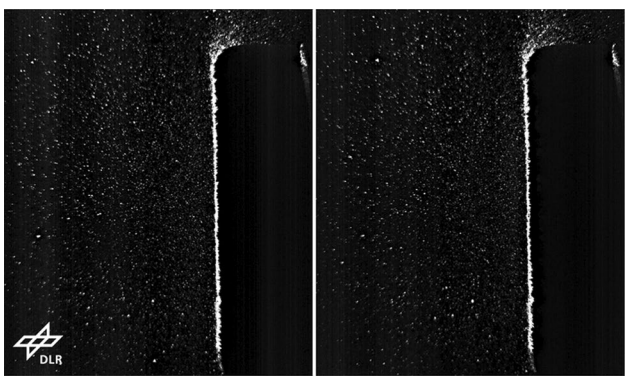

Fig. 7 Raw PIV data. Frame 1 on the left and frame 2 on the right. The flow comes from the left

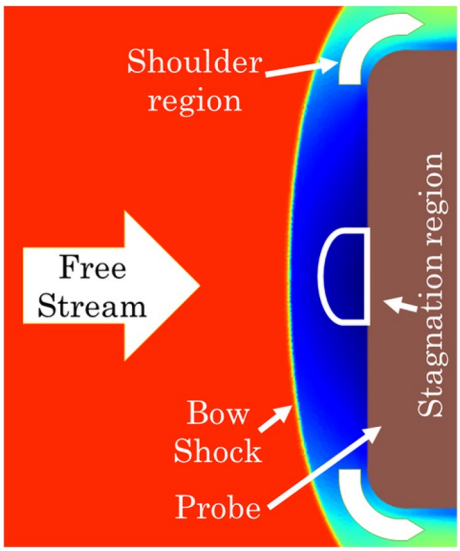

Fig. 8 Flow field features

Different zones present different characteristic velocities; with constant particle mass flow rate, this means that different zones present different particle seeding density. The very broad nature and characteristics of the observed particles in terms of velocity, size, and seeding density, pose a big challenge to the PIV evaluation, whose working principle is based on the cross-correlation algorithm within interrogation windows (IW). The most refined evaluation strategy would require a variable IW size, window deformation, exclusion of rebounded particles in the bow shock and in the free stream, multi-pass, tuned vector validation, and averaging. In the following, a simpler evaluation strategy is presented.

When PIV is performed in the vicinity of a surface (in this case the cork sample), the surface needs to be excluded from the result, by masking. From now on, pre-masking means computing the PIV result on a grid that excludes the non-relevant regions (like the cork sample), while post-masking means evaluating the PIV result on the whole image, and only then excluding the results computed on irrelevant regions.

It is observed that the PIV algorithm can break in the free stream, due to the high particle displacements of up to 100 px, and the relatively low seeding density: without adequate measures, the PIV algorithm can sometimes compute null velocities, where a 2 km/s velocity is expected. On the other hand, the shock region is easily computed, as its seeding density is higher and its particle displacement is lower. To increase the algorithm's robustness in the free stream, a constant initial window shift of 100 px in the direction of the main flow is given. However, such a high constant window shift applied to the whole flow field can create problems on the resolution of the shock. In fact, depending on the used computation strategy, the shock layer might shrink in the final result: the cross-correlation algorithm of PIV gets influenced by the initial large window shift that pushes the algorithm towards the computation of higher velocities in the shock layer. This effect is not observed if the post-masking strategy is chosen over the pre-masking one.

For these reasons, the PIV evaluation based on *multi-pass* with *window shift* and final averaging is performed in the whole image. Subsequently, the irrelevant zones are excluded (*post-masking*), namely the zone corresponding to the probe, the zone below the probe, and a small region in the bottom part of the image that is not sufficiently illuminated by the laser. The initial and final IW sizes of the multi-pass algorithm are set to 512×512 px^2 and 96×96 px^2, respectively, with 50% overlap. A constant initial guess on the horizontal shift is given as 100 px. The choice of window size is based on the seeding density of the free stream. More resolved analysis could be performed in the shock layer where the seeding density is higher.

Seeding quality varies with time: some pictures have perfect homogeneous seeding, some have only a region with good seeding, and some counted only few particles. For this reason, the correct choice of vector validation and filtering technique is crucial in data processing: all vectors with too low correlation peaks are excluded, and vector validation based on the 5×5 median filter is used, which is capable of rejecting groups of spurious vectors. Non-valid vectors are in this way removed and iteratively replaced. To avoid smoothing strong gradients introduced by the step-like velocity change over a bow shock, no interpolation is used in empty spaces. Due to the stringent criteria used by the validation algorithm, it is rare to find a picture where all vectors are computed: the results are in the end averaged over the whole dataset, to obtain a smoother result. Note that the sample geometry varies during the test, due to expansion, charring, ablation, and erosion. Thus, averaging might introduce errors on the shock layer velocity (and geometry) determination. However, this error is considered acceptable thanks to the relatively short test duration: during this phase, the probe deformation is considered negligible. It is worth noting that the sample exhibits slightly greater deformation in FCII^P compared to FCI^P.

3.3.2 General considerations

As for the experimental campaign presented in Salvi and Gülhan (2024), the depressurization process of the test chamber

does not compromise the stability or alignment of the laser line, which simplifies the calibration and the processing procedures. This is due to the robust structural design of the L2K facility and its relatively low mass flow rates. Also, the camera's focus is not affected by the chamber depressurization and no vibrations are observed.

Unlike the discussion presented in Salvi and Gülhan (2024), the presence of glowing particle agglomerates in the flow does not significantly affect the signal with the setup used. This positive effect is caused by the choice of a higher focal distance f of the cylindrical lens that generates the light sheet: the higher f generates a less dispersed light sheet, causing stronger illumination of the particles, thus higher signal-to-noise ratio.

In the L2K, the high-enthalpy flow is glowing itself, due to chemical reactions and high enthalpy. The glowing flow reduces the second frame's quality, due to its long acquisition time. Narrowband filters centred on laser's emission wavelength must be used, such as the one described before, centred on 532 nm and with $FWHM = 5$ nm. Using the long-distance microscope helps mitigate this issue.

3.4 Numerical setup

The comparison between flow velocity and particle velocity can give meaningful insights in the characteristic physical phenomena of the wind tunnel environment. For this reason, CFD computations were performed with the DLR-TAU flow solver to evaluate the expected flow velocity of the particle-free flow conditions (FC^{nP}). Note that the comparison between CFD and PIV is only valid under the assumption of one-way coupling between the flow and the particles—that is, the flow influences particle motion, but the particles do not affect the flow characteristics.

High-temperature effects and non-equilibrium chemistry were considered in the simulations: a 11-species/103-reactions chemical model is chosen for the chemical compounds $CO_2, CO, O_2, O, NO, N_2, N, C, C_2, CN, NCO$. Computations are performed in steady flow field and 2D axial symmetric geometry, with structured mesh layer on the probe surface and three-times adapted unstructured mesh in the free stream and shock layer. The convergence is assured by monitoring the density residual. The simulated flow core velocity of both flow conditions was validated in Salvi et al. (2023) with TDLAS, and the computed shock stand-off distance δ was validated in previous experimental campaigns without particles.

4 Results

In this section, the qualitative analysis of the sample behaviour is reported; then, the collected particles are analysed with SEM and EDX; PIV results are then reported, and in the end a comparison with particle-free CFD results is discussed.

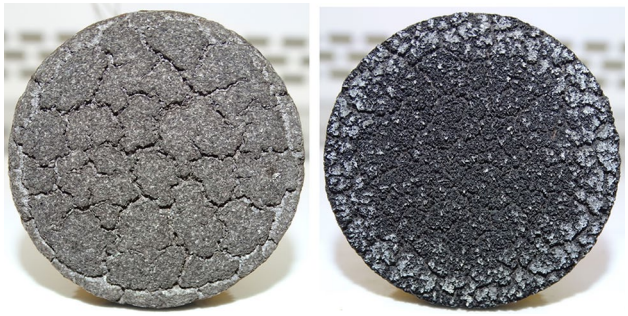

Fig. 9 Sample after testing in FCI without particles (left) and with particles (right)

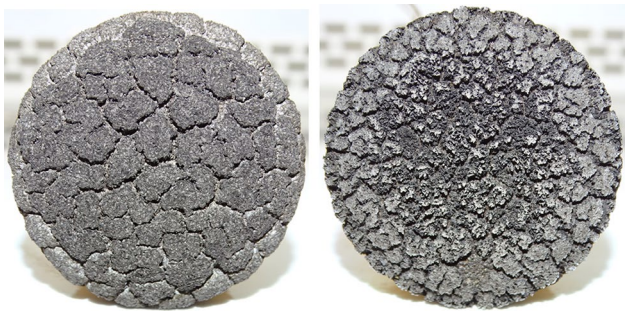

Fig. 10 Sample after testing in FCII without particles (left) and with particles (right)

4.1 Sample behaviour

The pictures of the samples taken after each test are reported in Figs. 9 and 10. The photographs on the left are relative to FC^{nP}, namely the tests without particles, while the ones on the right are relative to FC^{P}, namely the tests with particles.

One can observe that for FC^{nP} the sample surface develops a granular structure characterized by large cell-like patterns, which is due to charring. These cells tend to grow in size during the test, up to a point where their size stabilizes. This is a well-known behaviour of cork-based ablators, already observed in several experimental campaigns, such as in Sakraker et al. (2022). On the other hand, when particles are present in the flow, the cells are completely absent for FCI^{P} and present on a smaller extent in $FCII^{P}$. In fact, the cells are much smaller in $FCII^{P}$ than $FCII^{nP}$, and they are found only on the outer region of the samples. In the tests with particles, the surface looks rougher, and spikes are observable: the erosion effect caused by the particles impacting on the surface causes the rupture of the cells, detaching the surface layer of the sample and exposing the underlying layer, enhancing the recession phenomenon.

The impact location is stochastic, depending on the particle seeding density in the flow, and for this reason it is hard to recognize patterns on the eroded surface, contrarily to the case where particles are not seeded in the flow.

By comparing the samples before and after the tests without and with particles, it is observed that:

- In FCI^{nP}, the sample expands more than it ablates; thus, the ablation phenomenon is contained. Cells are visible.
- In FCII^{nP}, the sample experiences recession, meaning that the ablation process gains importance over the thermal expansion and charring. In this case, the ablation is more severe on the outer region of the front surface than in the centre. Cells are visible.
- In FCI^{P}, the erosion phenomenon prevails overall on the whole surface of the sample: the presence of particles causes recession, which was not observed in FCI^{nP}. Spikes are visible.
- In FCII^{P}, the erosion phenomenon prevails overall in the central region of the sample, where spikes are visible. The ablation process might prevail on the erosion process in the outer region of the front surface, showing the development of cells. The cells of FCII^{P} are nevertheless smaller than FCII^{nP}, showing that the rupture process of these patterns caused by particle impact is still playing a role.

The erosion phenomenon happens due to momentum transfer from the particle to the surface, which depends on the impact angle of the particle on the surface, among other parameters. According to the flow topology, a particle can hit the central region of the sample perpendicularly, while an impact on the outer region happens with a smaller angle, due to the curved profile of the sample. The smaller impact angle on the side provides less momentum transfer from the particle to the surface. The less prominent erosion observed in FCII^{P} on the outer region can be an evidence of this phenomenon.

4.2 Collected particles

SEM pictures of the collected particles are reported in Figs. 11 and 12, for FCI^{P} and FCII^{P}, respectively. For every analysed site, EDX analysis is performed to understand and verify the chemical composition of the observed object. The pictures can be compared with the control sample of MgO particles shown in Fig. 5.

The particles collected in FCI^{P} form a thick layer of solid material on top of the copper tape. This is due to sintering caused by the energy released on impact combined with the high temperature in the stagnation point. It is in fact hard to recognize particles in the reported picture, as their morphology changed on impact. However, a grainy structure of the sintered layer is visible, which supports the hypothesis that the particles might not have experienced a phase change during flight.

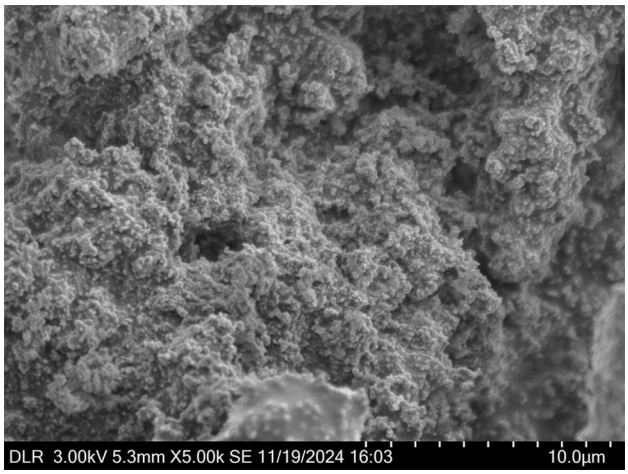

Fig. 11 Particles collected in FCI^{P}

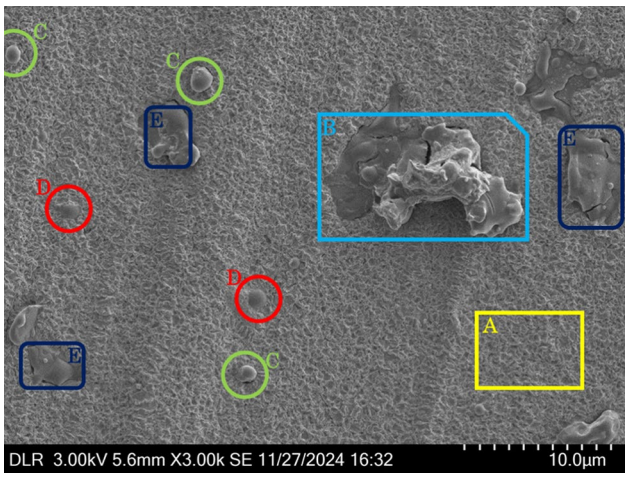

Fig. 12 Particles collected in FCII^{P}

The particles collected in FCII^{P} are instead subject to different phenomena. The picture shows different particles/chunks laying on a rough surface. The rough surface **A** is copper oxide, which is probably created after the reaction of carbon monoxide or atomic oxygen in the flow with the copper tape, whose glue layer evaporates in a fraction of a second. The big chunky structure in the middle of the image **B**, as well as the small spheres on the top left **C**, the darker small spots splashed on the copper oxide layer **D**, and the smoother regions on the bottom left and top right **E**, are made of MgO, namely the same species of the particles used during the tests. By comparing Fig. 12 with Fig. 5, one can observe that the morphology of particles has completely changed during the test, and it looks like they have

melted, most likely in the reservoir, where the temperature is higher than the melting temperature of MgO. Probably, the big chunk **B** was either fully solid or half molten before collision, the spherical agglomerate **C** was solid before collision, while the darker spots **D** were small molten spheres that splashed on impact, and the smoother regions **E** might have been large agglo-molten particles.

This technique presents further evidence of the hypothesis advanced in Salvi and Gülhan (2024), where it was assumed that in FCII^P particles can agglo-melt.[1] This phenomenon is not seen in FCI^P, where the total temperature is lower than the melting temperature of MgO, as reported in Table 1. The agglo-melting hypothesis is further supported by looking at the eroded probes in Fig. 9 and in Fig. 10 and at the PIV results presented in the following section. One can observe that that the eroded sample in FCII^P presents more cells than in FCI^P, possibly indicating that the amount of particles in FCII^P is reduced, eventually due to agglo-melting. In addition, the large agglo-molten particles might reside in the core part of the flow; therefore, more erosion is visible in the central area of the sample surface in FCII^P. It is anticipated here and confirmed later that the PIV results present higher fluctuations and uncertainty in the case of FCII^P, supporting the agglo-melting theory. Agglo-melting causes in fact a variation of the particle size distribution, which leads to a broad velocity range of different-sized particles. This reflects into larger fluctuations in the PIV results.

After studying several SEM pictures, it is hypothesized that the particles agglo-melt in the reservoir. Then, they cool down during the nozzle expansion and the free flight in the test chamber, probably experiencing another phase change as the free stream cools to approximately 600 K. It is impossible to say, though, if the particles re-solidify during this colder phase, as the process highly depends on the particle size and its characteristic flight time. It is difficult to estimate these values, since the particle size distribution varies due to the agglo-melting process in the reservoir that causes also a velocity dispersion of the different-sized particles.[2] Then, the particles enter the hot shock layer, heating up again before colliding with the sample.

Agglo-melting can occur both in the wind tunnel's reservoir and in front of the probe within the shock layer, where the flow temperature is higher than the particles' melting temperature. The characteristic length and residence time

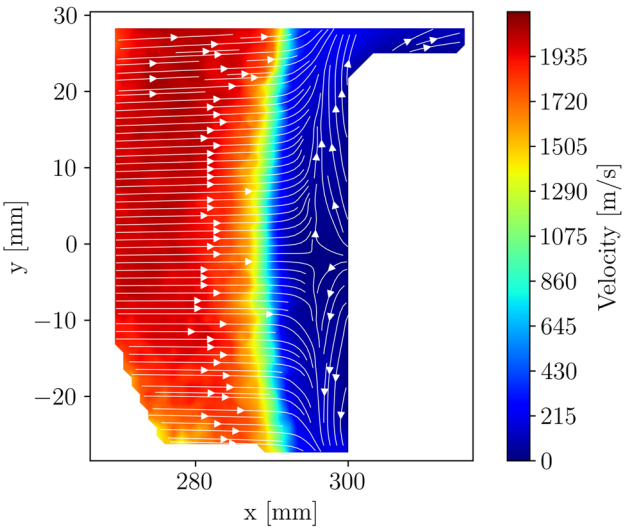

Fig. 13 PIV result FCI^P. The white region on the right is the cork sample. The flow comes from the left

of the particles in these high-temperature zones have an influence on the extent of the phenomenon. Future research should focus on determining whether these two parameters are comparable between wind tunnel conditions and the flight environment, to evaluate whether the agglo-melting phenomenon plays a role during actual flight. For example, particle trajectory simulations should be conducted for both the wind tunnel and flight environments. The results could be used to assess the residence time of particles in high-temperature regions and to compare the behaviour between the two conditions.

Note that this analysis is to be intended as a qualitative analysis only, due to the intrusive nature of the collection technique. Nevertheless, it is considered as a valuable first insight into the highly challenging topic of particle collection in high-enthalpy flows. Future studies could focus on the development of a probe that can collect particles without altering their properties.

4.3 PIV results

The final results obtained by averaging all the PIV images of one dataset are presented in the next figures. Figure 13 shows FCI^P, and Fig. 14 shows FCII^P. The results are presented with no smoothing, and the streamlines are plotted to highlight the behaviour in the shock region. The flow comes from the left. The large white mask on the right is the sample profile, while the small triangular mask on the bottom left is a region that is not sufficiently illuminated by the laser. One can observe different particle flow features, which are—from left to right—the free stream, the steep velocity decrease, and the shock layer region.

[1] Agglomerate due to melting.

[2] The flight time from the nozzle throat to the sample's surface (a 700-mm-long flight path) is in the order of hundreds of microseconds, if an average particle velocity between 1000 m/s and 2000 m/s is considered. Further investigation could be performed on the particles' thermal properties, to analyse the phase change's characteristic times and to characterize particles' behaviour in the wind tunnel.

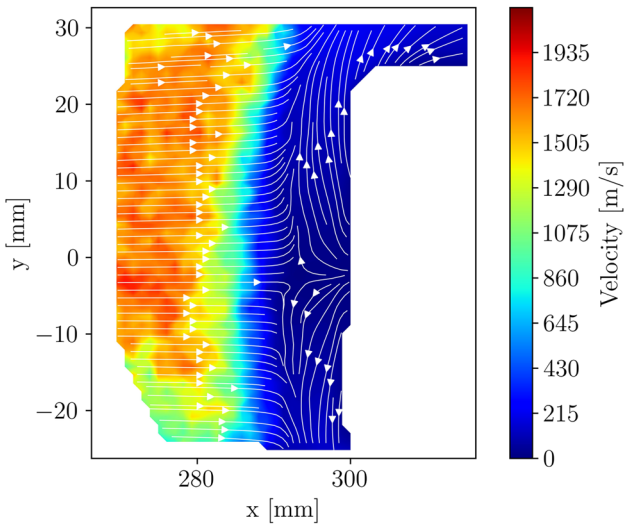

Fig. 14 PIV result FCII^P. The white region on the right is the cork sample. The flow comes from the left

FCI^P has generally smoother results than FCII^P. The reason lays in the seeding density and in the agglo-melting phenomenon described in Subsect. 4.2: due to the agglomeration, less particles are present in the flow, so the seeding density is lower in FCII^P. Moreover, the agglomeration leads to a size distribution change of the seeded particles, causing a velocity dispersion: bigger particles are less accelerated by the flow than smaller particles—this causes the higher enthalpy flow condition FCII^P to have a lower average particle velocity. For this reason, the PIV algorithm—which is highly influenced by the velocity of larger (and brighter) particles—evaluates more fluctuating results when the particle size is not homogeneous. In both results one can observe that the average velocity value of the particles in the free stream is about 2050 m/s in FCI^P and 1800 m/s in FCII^P. These results are slightly slower than the results presented in Salvi and Gülhan (2024), where the particle velocity in the free stream was measured by means of PIV in a more upstream region.

The shock layer's average velocity field is computed both in the stagnation point and in the shoulder region, where the flow expands to follow the probe's contour. It is interesting to see that for both flow conditions a region with counter-flow is present right on the surface of the probe. The counter-flow is believed to be due to different effects, namely the particles bouncing back after hitting the surface, the particles released due to probe's erosion, and the ones from probe's outgassing. For this reason, the stagnation point of the particle flow lays few millimetres upstream of the probe's surface. The detached position of the stagnation point might misleadingly suggest that particles do not impact the surface. However, it is important to note that the results shown represent an average, and the apparent detachment of the stagnation point could be caused by rebounded particles—that is, particles that have already impacted the probe.

In FCI^P the velocity gradient caused by the shock is well resolved. This region that has the highest velocity gradient is not to be intended as a fluid dynamic shock, since the particles exhibit a velocity lag relative to the flow. Thus, the actual shock location may differ. In FCII^P this region presents less smooth values, but the velocity decrease is nevertheless observed. To better visualize the velocity gradient, the velocity profiles along the axial coordinate x are reported for both flow conditions in Figs. 15 and 16 for FCI^P and FCII^P, respectively.

It is worth to see the data from another perspective, namely the fluctuations of the results. The fluctuations are

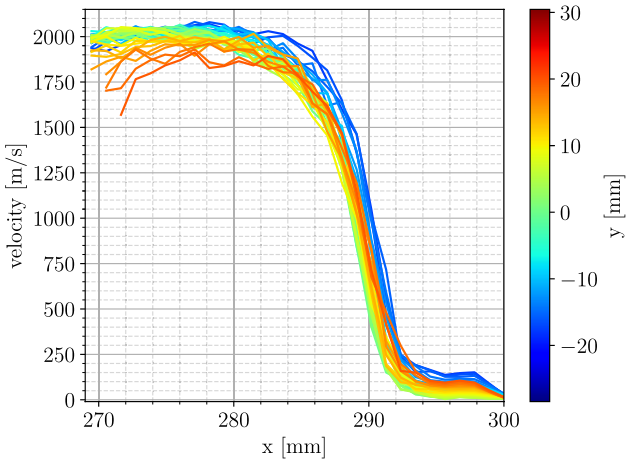

Fig. 15 Velocity profiles FCI^P

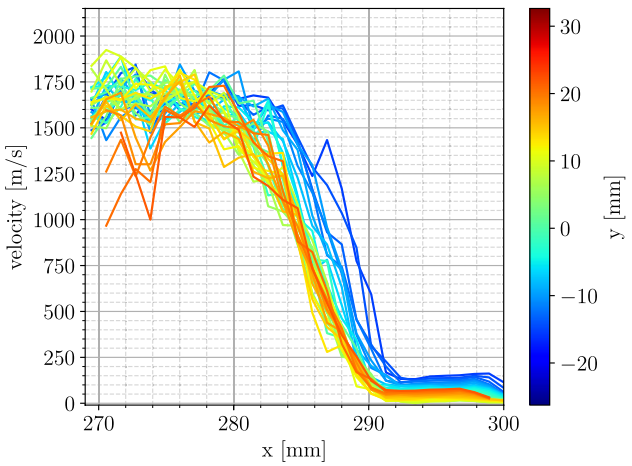

Fig. 16 Velocity profiles FCII^P

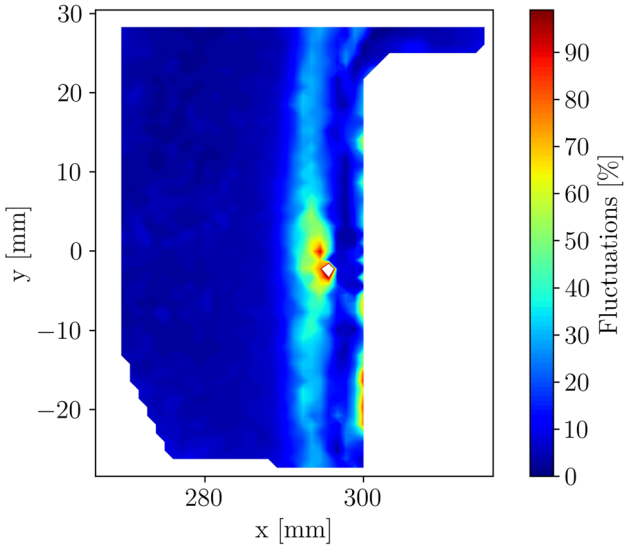

Fig. 17 Relative fluctuations FCI^P

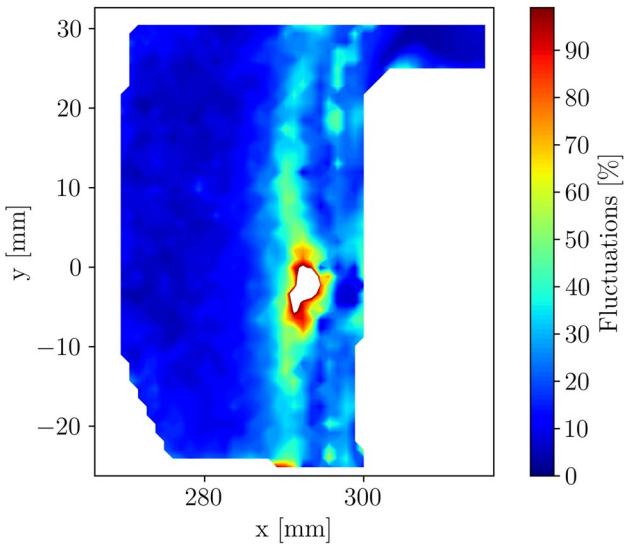

Fig. 18 Relative fluctuations $FCII^P$

evaluated through the relative uncertainty u_v, which is calculated as $u_v = \frac{\sigma/\sqrt{N}}{v}$; where σ is the standard deviation of the velocity after averaging the dataset, N is the number of valid samples, and v is the velocity magnitude. The fluctuations are presented in Figs. 17 and 18 for FCI^P and $FCII^P$, respectively, in terms of percentage.

For both flow conditions, the free stream and the part of the shock layer close to the sample present low fluctuations, which are prevalently below 10% for FCI^P and 20% for $FCII^P$. The region that bounds the flow and the counterflow presents fluctuations between 20% and 40%, and the region surrounding the stagnation point can be well above

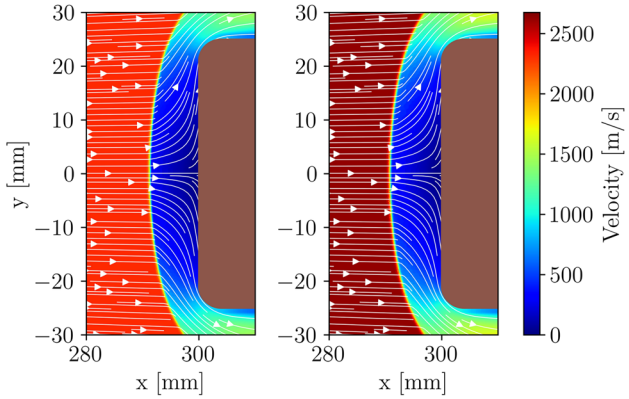

Fig. 19 Numerical simulation of the flow without particles. FCI^P on the left and $FCII^P$ on the right

70%. Around the stagnation point, which lays few millimetres upstream of the probe's surface, the fluctuations can be higher than 100%. In this region, the computed velocity is below 15 m/s, and the particles may exhibit reverse velocity components due to outgassing, erosion, and rebounding, leading to significant fluctuations in the results.

Note that PIV is most effective in flows where particles move coherently in the same direction within each interrogation window. However, near the stagnation point, this condition may not hold due to the coexistence of free stream particles with those that have rebounded, been eroded, or expelled by outgassing. This heterogeneous motion can lead to significant fluctuations in the result due to the PIV's cross-correlation algorithm. In future studies, PTV could be employed to track individual particles, thereby mitigating the limitations encountered when applying PIV in such complex flow regions.

4.3.1 Comparison with CFD

The simulations, zoomed in the relevant region of interest, are reported in Fig. 19, for both flow conditions.[3]

One can observe that:

- The computed wind tunnel free stream exhibits a high degree of homogeneity at the sample location, both

[3] In both cases, the Knudsen number evaluated with TAU is lower than 10^{-3} in the whole free stream region, as well as in the shock layer region upstream of the sample, confirming that the continuum assumption is valid in these regions. Within the actual shock, the Knudsen number can reach values up to 0.65; thus, the internal resolution of the shock is questionable. However, the relevant parameters for this analysis are the free stream velocity, the shock layer velocity, and the shock stand-off distance δ; thus, the uncertainty in the resolution of the shock is accepted.

in velocity magnitude and direction. The sample lies entirely within the homogeneous flow core.

- A comparison between CFD results (Fig. 19) and PIV measurements (Figs. 13 and 14) reveals several notable differences. While the free stream regions appear relatively uniform in both cases, a significant velocity lag—on the order of several hundred metres per second—can be observed between the particles and the expected flow velocity (as in Salvi and Gülhan (2024)). Another key discrepancy is seen in the shoulder region of the sample: CFD predicts velocities up to 1500 m/s, whereas PIV measurements do not exceed 500 m/s. This suggests that the particles are either unable to keep up with the rapidly expanding flow in that region, or that outgassing has generated a thick, slower-moving layer in which the particles are entrained.
- The counter-flow is not captured in the CFD simulations, as the setup does not account for outgassing or particle rebound phenomena. As a result, the stagnation point predicted by CFD differs from that observed in the PIV measurements: in the CFD, it lies on the probe surface, whereas in the PIV data, it is detached from the surface. This discrepancy suggests that the counter-flow observed in the PIV results is caused by the material response or by presence of particles.
- The CFD shock is much closer to the surface than the particle "shock", contrarily to what one may expect.

In future work, the validity of the one-way coupling assumption should be critically evaluated. This will require the development of a simulation setup capable of resolving particle trajectories and their rebound and outgassing phenomena, if necessary. Particle trajectories should be accurately simulated and tracked to capture their dynamic interaction with the flow.

More advanced numerical simulations should also aim to investigate the causes behind the discrepancy in shock stand-off distance δ observed between CFD and PIV results. The stand-off distance might be larger for PIV results due to the presence of counter-flow caused by material outgassing and particle rebounding. In addition, δ is influenced by the Mach number and gas composition, which in turn depend on pressure, temperature, density, viscosity, and flow chemistry—which governs the specific heat ratio γ. When particles are present in the flow, they can interact with it through various mechanisms: **momentum exchange**, due to drag forces resulting from velocity lag; **energy transfer**, through convective and radiative heating or cooling as well as potential phase changes; and **chemical reactions**, where particles may act as catalytic surfaces, altering the flow chemistry. All these phenomena can influence the thermodynamic state, composition, and momentum of the gas, potentially altering the shock position—either bringing it closer to or moving it farther from the probe. This variation becomes more pronounced with increasing particle density. Future studies should investigate whether these effects play a significant role in modifying the flow properties or whether they remain negligible, thereby invalidating or supporting the assumption of one-way coupling.

Furthermore, future research should aim to apply PIV around water-cooled steel (or copper) samples with the same geometry as the cork samples used in this study. This configuration eliminates the outgassing phenomenon, allowing for a direct comparison with the current results to determine whether outgassing or particle rebound plays the dominant role in the observed counter-flow behaviour. The outcome of this comparison will provide valuable insights for developing efficient and physically meaningful numerical setups.

5 Conclusions

This study is the continuation of the experiment presented in Salvi and Gülhan (2024), where 2D-2C PIV was implemented in the L2K arc-heated wind tunnel to characterize its particle flow field. In this work, the particle-laden flow around cork samples is characterized by means of particle collection after impact and 2C-2D PIV. To the knowledge of the authors, this research represents the first implementation of PIV around a sample in an arc-heated wind tunnel. The samples are studied in four flow conditions, reported in Table 1, namely the low-/high-enthalpy ones (I/II) and the ones with/without particles (*P/nP*), designed to simulate conditions encountered during Martian atmospheric entry. Particle erosion is observed and qualitatively presented in Subsect. 4.1.

Collected particles gave further insight in the characterization of the L2K's particle-laden flow; they are shown and discussed in Subsect. 4.2, and compared with the control sample of particles before the test: a considerable morphological change of the particles was observed during their flight in the wind tunnel. Thanks to the collected particle samples, new evidence confirming the hypothesis of agglo-melting advanced in Salvi and Gülhan (2024) was found, for $FCII^P$. **Agglo-melting** is the short term used in the paper to express the agglomeration of the particles due to melting. The particles do not undergo the same melting phenomenon in FCI^P, as expected, since the total temperature of this flow condition is lower.

The particle velocity in the free stream and in the shock layer is measured, ranging from 2100 m/s to 0 m/s. Several particle flow features are observed, such as the particle's steep velocity gradient across the shock, the shock layer, and a counter-flow that might be due to outgassing and rebounded particles. The PIV evaluation strategy is reported in Subsect. 3.3.1, along with a discussion about

the different kinds of particles that one can observe in the region of interest. PIV results are reported in Figs. 13 and 14 and in the following figures. The PIV results are compared with numerical simulations of the particle-free flow shown in Fig. 19, only in terms of shock stand-off distance and overall velocity, assuming one-way coupling between flow and particles. Generally, a significant velocity lag between flow and particles is to be expected in these flow conditions, and a discrepancy in terms of stand-off distance was observed. Future work is required for the improvement of numerical simulations, to address the reason of the stand-off distance discrepancy and to define whether the one-way coupling assumption can be considered valid.

5.1 Outlook

This study represents the first PIV analysis on a stagnation sample in an arc-heated wind tunnel for TPS testing, proving the technique feasible and opening the gates to future similar experiments dedicated to the study of the effects caused by particle-laden high-enthalpy flows on thermal protection systems. In the future, particle tracking algorithms should be used to better resolve particle velocity in the highly complex region in front of the bow shock, where particles with reverse velocity components coexist.

After this analysis, it is clear how challenging it will be to collect particle samples for the purpose of measuring particle sizes, which is important to validate numerical tools for the simulation of such flows. Future studies should focus on the development of a probe for particle collection in high-enthalpy flows, for the purpose of particle characterization. Additional experimental techniques should be used for the purpose of particle size determination, such as phase Doppler particle analyser (PDPA).

The particle size distribution cannot be considered unvaried from the insertion of the particles in the wind tunnel to their arrival on the sample's surface, as the agglo-melting phenomenon can happen, depending on the total flow temperature. These observations raise the urge to consider this phenomenon in numerical models. For instance, two molten colliding particles should continue their trajectory in the flow in a bonded configuration—an "agglo-molten tandem"—after the anelastic collision.

Moreover, the observation of agglo-melting raises awareness to consider this phenomenon when designing a heat shield, as it leads to changes in particle properties: particles entering the bow shock might experience phase change, anelastic collision, and agglomeration, leading to a potential increased erosion capability of the particles due to their increased inertia, momentum, and thermal inertia. This might have an effect on the heat shields used during atmospheric entry. It is however unclear if this phenomenon is relevant in flight, because the residence time of a particle in the hot flow region (shock layer) might differ from the residence time of a particle in the hot zones of the L2K (settling chamber and shock layer). Further analysis is needed regarding this aspect.

Acknowledgements The authors would like to thank Prof. Isaac Boxx from RWTH Aachen for his valuable scientific inputs, Amorim Cork Composites for providing the samples for free, and the staff from the Supersonic and Hypersonic Technologies Department in DLR Köln, in particular Dominik Neeb and Pawel Goldyn.

Author contributions CS contribution to this work includes methodology, design, engineering, formal analysis and investigation, original draft preparation and editing. AG defines as supervisor, the research content, and necessary resources.

Funding Open Access funding enabled and organized by Projekt DEAL. This project is funded by the DLR's Program Directorate for Space Research and Development.

Data availability There are no research data outside the submitted manuscript file.

Declarations

Conflict of interest The authors declare that they have no known competing financial interests or personal relationships that could have appeared to influence the work reported in this paper.

Ethical approval Not applicable.

Consent to participate No special consent required for participation.

Consent for publication No special consent required for publication.

References

Allofs D, Neeb D, Gülhan A (2022) Simultaneous determination of particle size, velocity, and mass flow in dust-laden supersonic fows. Exp Fluids 63:64

Allofs D, Neeb D, Gülhan A (2023) Particle mass flow determination in dust-laden supersonic flows by means of simultaneous application of optical measurement techniques. Exp Fluids 64:49

Allofs D, Neeb D, Gülhan A (2023) Experimental investigation of heating augmentation by particle kinetic energy conversion in dust-laden supersonic fows. Exp Fluids 64:179

Amorim Cork Composites (2025) https://amorimcorksolutions.com/en-us/. Accessed: 01-01-2025

Bade WL, Yos JM (1975) The NATA Code - Theory and Analysis. Report CR-2547, NASA

Buntrock LJ, Grabe M, Fischer H (2023) Contamination assessment of a freely expanding green propellant thruster plume. IOP Conf Series Mater Sci Eng 1287:012044

ESA. ExoMars (2016) Schiaparelli Descent Sequence. https://exploration.esa.int/web/mars/-/57465-exomars-2016-schiaparelli-descent-sequence. Accessed: 22-07-2022

DLR, ESA (2006) Experimental and theoretical study of Mars dust effects, heat transfer measurement report. Report MDUST-DLR-TN-032, Supersonic and Hypersonic Technologies Department, DLR, Köln

Kessel PA (1987) Rocket exhaust probe. US Patent 4,662,216

Langton M, Hermansson A (1973) Image analysis determination of particle size distribution. Food Hydrocolloids 7:11–22

Palmer G, Ching E, Ihme M, Allofs D, Gülhan A (2020) Modeling heat-shield erosion due to dust particle impacts for Martian entries. J Spacecr Rocket 57:857–875

Palmer G, Sahai A, Allofs D, Gülhan A (2022) Comparing particle flow regimes in the l2k arcjet with Martian entry conditions. In *2nd International conference on flight vehicles, aerothermodynamics and re-entry missions and engineering*, Heilbronn, 19-23 Jun

Raffel M, Willert CE, Scarano F, Kähler CJ, Wereley ST, Kompenhans J (2018) Particle Image Velocimetry - A Practical Guide, 3rd edn. Springer International Publishing AG, Cham, Switzerland

Saile D, Allofs D, Kühl V, Riehmer J, Steffens L, Gülhan A (DLR AS-HYP), Beversdorff M, Förster W, Willert C (DLR AT-OTM), Carlotti S, Maggi F (SPLab, Polimi), Liljedahl M, Wingborg N (FOI). Experimental modeling of alumina particulate in solid booster: Final Report. Report ESA Contract No. 4000114698/15/NL/SFe, German Aerospace Center (DLR), Department of Supersonic and Hypersonic Technologies, Köln, DE, (2020)

Sakraker I, Chazot O, Carvalho JP (2022) Performance of cork-based thermal protection material P50 exposed to air plasma. CEAS Space J 15:377–393

Salvi C, Gülhan A (2024) Velocity measurements in particle-laden high-enthalpy flow using non-intrusive techniques. Exp Fluids 65:39

Salvi C, Steffens L, Hohn O, Gülhan A, Maggi F (2023) Martian flow characterization using tunable diode laser absorption spectroscopy, in high enthalpy facilities. Acta Astronautica 213:204–214

Wang S, Wang Y, Ramasse Q, Fan Z (2020) The nature of native MgO in Mg and its alloys. Metall Mater Trans A 51A:2957-2974

Authors and Affiliations

Ciro Salvi[1] · Ali Gülhan[1]

✉ Ciro Salvi
ciro.salvi@dlr.de

Ali Gülhan
ali.guelhan@dlr.de

[1] Supersonic and Hypersonic Technologies Department, German Aerospace Center (DLR), Linder Höhe, Köln 51147, Germany